An Iterative Linear Method for Estimating the Stress Tensor from Earthquake Focal Mechanism Data: Method and Examples

Eric Beaucé[a], Michel Campillo[b,a], Robert D. van der Hilst[a]

[a] *Department of Earth, Atmospheric, and Planetary Sciences, Massachusetts Institute of Technology, Cambridge, MA, United States*
[b] *Institut des Sciences de la Terre, Université Grenoble Alpes, Grenoble, France*

Abstract

Earthquake focal mechanism data provide information about the stress state at the origin of these earthquakes. The inversion methods that are commonly used to infer the stress tensor from focal mechanisms have varying complexity but always rely on a number of assumptions. We present an iterative method built upon a classic linear stress tensor inversion that allows to relax the assumption on shear stress magnitudes while preserving the computational simplicity of the linear problem. Every iteration of our method computes the least-squares solution of the problem, which makes the method fast enough to estimate the inverted parameter errors with non-parametric resampling methods such as bootstrapping. Following previous studies, this method removes the fault plane ambiguity in focal mechanism data by selecting the set of nodal planes that best satisfies the Mohr-Coulomb failure criterion. We first illustrate the performance of the proposed method on synthetic and real data sets, and then discuss the relationship between the assumption of constant shear stress magnitudes and the presence of non-optimally oriented faults. We provide the Python package ILSI to implement the proposed method.

1. Introduction

The sense of motion on faults carries information on the stress state surrounding these faults. Field measurements of fault orientations and slip directions (slickensides) were first used to retrieve the stress tensor using a number of assumptions [*e.g.* Carey et al., 1974; Angelier, 1979; Angelier et al., 1982]. The cornerstone assumption of these methods is that slickensides are oriented along the direction of maximum shear stress resolved on the faults [the so-called Wallace-Bott assumption, Wallace, 1951; Bott, 1959]. Stress tensor inversion techniques were extended to the more widely available earthquake focal mechanism data, which describe faulting from seismic observations instead of direct field measurements. In general, the inverse problem is non-linear and solving it requires grid-search or other global optimization methods [Angelier et al., 1982; Gephart and Forsyth, 1984], but with additional assumptions the problem can be linearized [*e.g.* Michael, 1984]. Both non-linear and linear inversion techniques suffer from the ambiguity in earthquake focal mechanism data that provide two possible fault planes per datum, without offering the possibility to identify the actual fault plane [the consequences of choosing the wrong plane are discussed at length in Michael, 1987]. While some of the non-linear inversion methods choose the fault planes as the set of planes that

minimize their objective function [such as the algorithm implemented in Focal Mechanism Stress Inversion, FMSI, Gephart, 1990], other criteria, physics-based and independent from the objective function, are preferred to avoid data over-fitting. Lund and Slunga [1999] introduced the use of the Mohr-Coulomb failure criterion to select fault planes. In this work, we present an inversion method built upon the linearized problem due to Michael [1984], turning it into an iterative inversion while preserving the computational efficiency of the least-squares solution of a linear problem. We thus relax the assumption made by Michael [1984] that shear stress magnitude is constant across faults or, equivalently, that all faults are optimally oriented within the stress field. We also use the Mohr-Coulomb failure criterion to select fault planes. The proposed method is implemented by our Python package ILSI (Iterative Linear Stress Inversion, see Data and Resources).

In Section 2, we review the previous work on the topic on stress inversion and introduce our method. Section 3 demonstrates the advantages of the proposed method with synthetic data sets, and Section 4 shows its performances on real data sets. Finally, we discuss the implications of the assumption on shear stress magnitudes in Section 5.

2. Methodology

2.1. Previous Work

Given a fault plane with orientation described by its unitary normal $\hat{n}$, the traction on the plane is:

$$T = \sigma\hat{n}, \tag{1}$$

where σ is the Cauchy stress tensor, and T is the traction. The normal T_n and tangential (shear) T_t components of the traction are:

$$\begin{aligned} T_n &= (\sigma\hat{n}\cdot\hat{n})\hat{n} = \sigma_n\hat{n} \\ T_t &= T - T_n = \sigma\hat{n} - (\sigma\hat{n}\cdot\hat{n})\hat{n} = \tau\hat{t}. \end{aligned} \tag{2}$$

In Equation (2), σ_n and τ are the magnitudes of the normal and shear tractions, respectively. The direction of shear traction is given by the unitary vector $\hat{t}$. The stress tensor is often represented by its eigendecomposition: the principal stress directions $\hat{\sigma}_i$ (eigenvectors) and the principal stresses σ_i (eigenvalues, $i = 1, 2, 3$). A plane that is perpendicular to $\hat{\sigma}_i$ does not experience any shear, and is under a purely compressional traction of magnitude σ_i. By convention, eigenvalues are ordered such that σ_1 is the most compressional stress, σ_3 is the least compressional stress and σ_2 is the intermediate stress. Note that in the earth all stresses are compressional because of lithostatic pressure, and extensional stresses only exist in the sense of deviatoric stresses (the stress minus the lithostatic pressure).

Stress tensor inversion of earthquake focal mechanism data relies on two assumptions:

- the stress tensor is homogeneous in space,
- slip on faults occur in the direction of maximum resolved shear stress [Wallace-Bott assumption, Wallace, 1951; Bott, 1959].

An earthquake focal mechanism is a descriptor of the orientation and slip direction of a fault, based on the radiation pattern of seismic waves. Because of the symmetry of radiation patterns, there exists two fault planes with different slip directions that describe the same focal mechanism. Thus, each focal mechanism datum provides two fault normals $\hat{n}$ and two slip directions $\hat{s}$. We describe later a way of solving this ambiguity, but will assume for now that the fault plane and slip direction are known. Based on the Wallace-Bott assumption, one seeks the stress tensor that predicts shear directions $\hat{t}$ that best match the slip directions $\hat{s}$. This inverse problem does not provide any information on the absolute stress magnitudes, therefore it can only retrieve the reduced stress tensor, *i.e.* a normalized deviatoric stress tensor σ^*:

$$\mathrm{Tr}(\sigma^*) = \sum_{k=1}^{3} \sigma^*_{kk} = 0; \qquad \sum_{i,j} (\sigma^*_{ij})^2 = 1. \tag{3}$$

For simplicity, hereinafter we keep using σ instead of σ^*. One can only obtain four independent parameters from the inverse problem: the three principal stress directions $\hat{\sigma}_i$, and the shape ratio R,

$$R = \frac{\sigma_1 - \sigma_2}{\sigma_1 - \sigma_3}. \tag{4}$$

This scalar quantity is a measure of the relative magnitude of the principal stresses. In terms of deviatoric stress, if $R > 0.5$, σ_2 is extensional, and conversely if $R < 0.5$ then σ_2 is compressional. One can think of R as describing the position of σ_2 in between σ_1 and σ_3 on the x-axis of a Mohr circle (see Figure 1).

For a population of faults described by their normals $\hat{n}_i$ and their slip directions $\hat{s}_i$, writing Equation (2) for each fault and identifying the shear direction $\hat{t}_i$ to the slip direction $\hat{s}_i$ yields the following system of equations for shear tractions:

$$\sigma\hat{n}_i - (\sigma\hat{n}_i \cdot \hat{n}_i)\hat{n}_i = \tau_i \hat{s}_i. \tag{5}$$

The inverse problem consists of finding σ such that Equation (5) is satisfied on each fault i. Unfortunately, even though the left-hand side of Equation (5) is linear in σ, the right-hand side is not because of the shear magnitude τ_i. Although one cannot determine the absolute shear magnitudes, the relative magnitudes between faults still matter. Several strategies have be taken to solve the inverse problem: Angelier et al. [1982] solve the non-linear problem iteratively, and the broadly used method due to Gephart and Forsyth [1984] adopts a grid-search over the four independent parameters to minimize their angular misfit (*i.e.* their objective function does not depend on shear magnitudes). These two methods consider errors not only in the slip directions but also in the orientation of the fault normals. The other widely used method is due to Michael [1984], which stands out by its simplicity, and which many other methods are built upon [for example, Hardebeck and Michael, 2006; Martínez-Garzón et al., 2014]. The author made the assumption that shear stress is relatively constant from fault to fault, thus assigning the shear magnitude on the right-hand side of Equation (5) a scalar (equal to one). We discuss the implications of the assumption on shear stress magnitudes in Section 5. The linear problem is:

$$Gm = d \quad (6)$$

$$\underbrace{\begin{pmatrix} & & & & \\ \hat{n}_{i,1} + \hat{n}_{i,1}\hat{n}_{i,3}^2 - \hat{n}_{i,1}^3 & \hat{n}_{i,2} - 2\hat{n}_{i,2}\hat{n}_{i,1}^2 & \hat{n}_{i,3} - 2\hat{n}_{i,3}\hat{n}_{i,1}^2 & \hat{n}_{i,1}\hat{n}_{i,3}^2 - \hat{n}_{i,1}\hat{n}_{i,2}^2 & -2\hat{n}_{i,1}\hat{n}_{i,2}\hat{n}_{i,3} \\ \hat{n}_{i,2}\hat{n}_{i,3}^2 - \hat{n}_{i,2}\hat{n}_{i,1}^2 & \hat{n}_{i,1} - 2\hat{n}_{i,1}\hat{n}_{i,2}^2 & -2\hat{n}_{i,1}\hat{n}_{i,2}\hat{n}_{i,3} & \hat{n}_{i,2} + \hat{n}_{i,2}\hat{n}_{i,3}^2 - \hat{n}_{i,2}^3 & \hat{n}_{i,3} - 2\hat{n}_{i,3}\hat{n}_{i,2}^2 \\ \hat{n}_{i,3}^3 - \hat{n}_{i,3} - \hat{n}_{i,3}\hat{n}_{i,1}^2 & -2\hat{n}_{i,1}\hat{n}_{i,2}\hat{n}_{i,3} & \hat{n}_{i,1} - 2\hat{n}_{i,1}\hat{n}_{i,3}^2 & \hat{n}_{i,3}^3 - \hat{n}_{i,3} - \hat{n}_{i,3}\hat{n}_{i,2}^2 & \hat{n}_{i,2} - 2\hat{n}_{i,2}\hat{n}_{i,3}^2 \\ & & & & \end{pmatrix}}_{G} \underbrace{\begin{pmatrix} \sigma_{11} \\ \sigma_{12} \\ \sigma_{13} \\ \sigma_{22} \\ \sigma_{23} \end{pmatrix}}_{m} = \underbrace{\begin{pmatrix} \\ \\ \hat{s}_{i,1} \\ \hat{s}_{i,2} \\ \hat{s}_{i,3} \\ \\ \\ \end{pmatrix}}_{d}$$

In Equation (6), d is the stack of all slip vectors and G is the stack of all matrices relating the stress tensor elements to the direction of shear stress on the faults. Given that we can only retrieve the deviatoric stress tensor (see Equation (3)), the last diagonal term that does not appear in Equation (6) is implicitly defined by $\sigma_{33} = -\sigma_{11} - \sigma_{22}$. The linear inverse problem defined by Equation (6) is usually solved in the least-squares sense, for example with the Tarantola and Valette formula [Tarantola and Valette, 1982]:

$$m = m_{\text{prior}} + \left(G^T C_D^{-1} G + C_M^{-1}\right)^{-1} G^T C_D^{-1} \left(d - G m_{\text{prior}}\right). \quad (7)$$

In Equation (7), m_{prior} is an approximate solution known a priori, C_D and C_M are the covariance matrices modeling the prior knowledge on the data and model parameter distributions, respectively. If no prior knowledge on the target solution is available, then $C_M^{-1} = 0$ and $m_{\text{prior}} = 0$. Note that this linear formulation only considers errors in slip directions and not in fault orientations.

2.2. This Study

We relax the assumption on constant shear stress magnitudes in Michael [1984] by iteratively solving for both the stress tensor elements and the shear stress magnitudes. The algorithm is:

1. Initialize the solution:
$$m^{(0)} = \left(G^T C_D^{-1} G + C_M^{-1}\right)^{-1} G^T C_D^{-1} d^{(0)} \quad (8)$$

2. Compute shear stress magnitudes at iteration t and update the set of linear equations (*i.e.* update the estimate of the right-hand side of Equation (5)):
$$\tau_i^{(t)} = |\sigma^{(t)}\hat{n}_i - (\sigma^{(t)}\hat{n}_i \cdot \hat{n}_i)\hat{n}_i|; \qquad d_i^{(t)} = \tau_i^{(t)} d^{(0)} \quad (9)$$

3. Solve the updated linear inverse problem and update the stress tensor elements $m^{(t)}$ using the previous estimate $m^{(t-1)}$ as prior knowledge:
$$m^{(t)} = m^{(t-1)} + \left(G^T C_D^{-1} G + C_M^{-1}\right)^{-1} G^T C_D^{-1} \left(d^{(t)} - G m^{(t-1)}\right). \quad (10)$$

4. Repeat 2 and 3 until $|\tau^{(t)} - \tau^{(t-1)}|$ is lower than a user-provided threshold.

The superscript in parenthesis is the iteration index, $d^{(0)}$ are the unitary slip vectors and C_M^{-1} is generally set to zero. C_D^{-1} can be used to give more or less weight to the observations based on their quality, or is equal to identity if all focal mechanisms are equally accurate. In Section 3, we show how this iterative procedure helps find the exact solution in synthetic examples. In this study, we use the outward footwall normals, and the slip direction of the hanging walls with respect to the footwalls, implicitly setting our stress tensor sign convention to *negative compression* (see Appendix Appendix A). The formula relating strike/dip/rake to normal and slip vectors can be found, for example, in Chapter 4.2 of Stein and Wysession [2009].

When dealing with earthquake focal mechanism data sets, one needs to determine the fault planes out of the pairs of nodal planes in order to get an accurate estimate of the stress tensor [Michael, 1987, illustrate how choosing the wrong planes impacts the solution]. We use the Mohr-Coulomb failure criterion to assess which planes are more likely to be the fault planes for a given stress tensor [Lund and Slunga, 1999]. We recall that this criterion states that a rupture occurs if the shear stress exceeds a critical value given by:

$$\tau_c = C + \mu\sigma_n, \tag{11}$$

where C and μ are the cohesion and the friction on the fault, respectively. We denote the effective normal stress on the fault by σ_n, meaning that we include any pore pressure in this term. The closer the shear stress τ is to the critical value, the more unstable the fault is. Therefore, a measure of fault instability is:

$$\Delta\tau = \tau - \tau_c = \tau - C - \mu\sigma_n = \tau - \mu(\sigma_n + C/\mu) = \tau - \mu\sigma_n^*. \tag{12}$$

In Equation (12), $\Delta\tau$ is the instability parameter as defined in Lund and Slunga [1999]. Note that we included cohesion into the normal stress magnitude ($\sigma_n \rightarrow \sigma_n^*$). Since we do not have access to absolute values of stress, the cohesion is not a relevant variable in this analysis. This also means that $\Delta\tau$ as defined here only has a meaning in a relative sense, when comparing different planes. Therefore, following Vavryčuk et al. [2013], Vavryčuk [2014], we express normal stresses with respect to the maximum compression stress σ_1, and normalize the instability parameter by its value at the most unstable plane. The modified instability parameter I is defined as:

$$I = \frac{\tau - \mu(\sigma_1 - \sigma)}{\tau_c - \mu(\sigma_1 - \sigma_c)}. \tag{13}$$

This formula was derived assuming *negative compression* (*i.e.* $\sigma_1 < \sigma_2 < \sigma_3$) for consistency with the first part of the method. τ_c and σ_c are the shear stress and normal stress magnitudes of the most unstable fault. The different terms of Equation (13) are defined graphically in Figure 1.

The shear stress magnitudes are always assumed positive in Equation (13), however when choosing the fault plane out of the two nodal planes of each focal mechanism, we need to take into account the direction of the shear stress with respect to the slip direction. Therefore, we multiply the instability parameter I by the sign of the dot product between shear stress and slip:

$$\tilde{I} = I \times \text{sign}\left(\hat{s} \cdot \hat{t}\right). \tag{14}$$

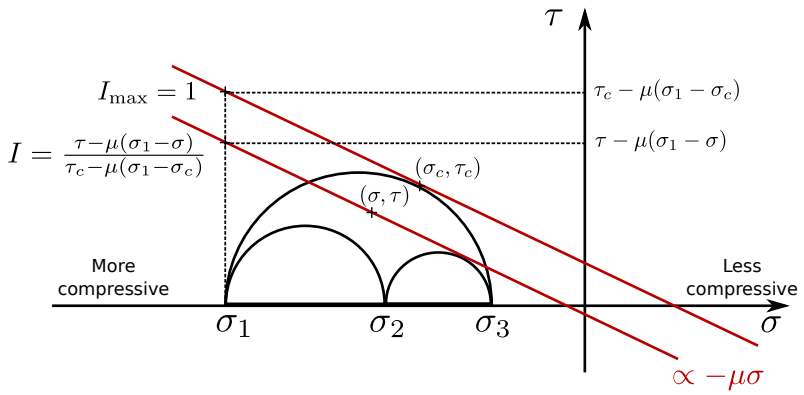

Figure 1: Definition of the instability parameter [Equation (13), following Vavryčuk et al., 2013] in the Mohr space with the *negative compression* convention. The red straight lines are the failure lines whose slopes are controlled by the friction μ. The most unstable fault has coordinates (σ_c, τ_c) in the Mohr space. The σ_i's are the principal stresses ordered from most compressive to least compressive.

Given a stress tensor σ, the fault plane that is chosen is the one that maximizes $\tilde{I}$ out of the two nodal planes.

Finally, the inversion includes the following steps:

1. Initial guess of σ by randomly selecting sets of nodal planes.
2. Choose the fault planes based on $\tilde{I}$.
3. Inner loop: Iteratively run the linear inversion (Equations (8)-(10)).
4. Repeat 2 and 3 until convergence or a user-defined maximum number of iterations.

Ten iterations are usually sufficient to reach convergence. Even though adding these two layers of iterations to the linear inversion from Michael [1984] makes our algorithm slower, it is still fast enough to be run many times on bootstrapped data sets to infer the parameter confidence intervals [Efron and Tibshirani, 1986]. We use this non-parametric method to estimate uncertainties in the applications described in the next sections.

We note that this algorithm may fail to converge in certain situations in which we observe an oscillatory solution. Given the stress tensor $\tau^{(i)}$ at iteration i, the selected set of nodal planes $\mathcal{S}^{(i)}$ depends on the outcome of the instability criterion $\tilde{I}(\tau^{(i)})$. Inverting this set of nodal planes produces a new stress tensor $\tau^{(i+1)}$ that, in turn, selects a new set of nodal planes $\mathcal{S}^{(i+1)}$. The discrete nature of $\mathcal{S}$ implies that any change in the selected nodal planes translates into a sharp change in the associated fault normals. Because shear stress is a smooth function of the fault normal (Equation (2)), it also implies a sharp change in the inverted stress tensor. Despite oscillations of the solution, one can still use this iterative procedure to explore different possible populations of faults, and select in the end the stress tensor that produces the lowest residuals. Ten iterations are again usually sufficient to explore the candidate solutions and select the best one.

3. Synthetic Experiments

We first test our method on synthetic data sets. The first experiment involves a stress tensor with northwest-southeast maximum compression, southwest-northeast least compression and vertical intermediate stress, favoring right-lateral strike-slip faulting on vertical east-west faults, or left-lateral strike-slip on north-south faults. The shape ratio is $R = 0.5$. The 100 fault planes are randomly distributed around azimuth 110° and the dips range from 65° to 90° (see leftmost column in Figure 2). Rake directions are in the direction of the shear tractions determined by the stress tensor in order to be fully consistent with the Wallace-Bott assumption. These strikes/dips/rakes are referred to as the "true fault planes" hereafter. Empirical parameter distributions are estimated by bootstrapping the original data set 1000 times. Confidence intervals are derived from these distributions.

Inverting the true fault planes (that is, without the need of inferring the fault plane) shows that the linear inversion does not retrieve the correct solution when using perfect data. The true solution is also not within the 95% confidence interval. In contrast, our iterative method finds the true stress directions and shape ratio. The inability of the linear method to find the true solution on perfect data is due to the erroneous assumption that all shear stress magnitudes are the same. In this synthetic experiment, there is actually a factor seven between the largest and the smallest shear magnitude values (see Figure 3). Figure 3 shows that the iterative method recovers the exact shear magnitudes while the linear method predicts incorrect values. The low shear stress magnitudes seen in Figure 3 are indicative of non-optimally oriented faults. We discuss in Section 5 how relaxing the assumption of constant shear stress magnitudes helps deal with these non-optimally oriented faults.

To test the efficacy of the fault plane selection criterion, we augment the data set with the auxiliary planes to synthesize a focal mechanism data set, and we vary the level of noise in the strike/dip/rake values. Even in the noise-free setting, getting the true solution is not trivial because the true fault planes are unknown. We compare four methods: the linear method, the linear method with the failure criterion, the iterative method, and the iterative method with the failure criterion. The latter is the method we introduced in Section 2.2, and is labeled as "Iterative failure criterion" in the figures. Figure 2 summarizes the results. Both in the noise-free and the low noise case, our method is the only one to retrieve the true solution. All methods fail in the high noise experiment, but even then our method produces a shape ratio distribution that indicates that the true shape ratio is a likely solution.

We do the same exercise with a second synthetic data set in which the dominant faulting style is oblique strike-slip with a normal component, and the shape ratio is $R = 0.7$. The 100 fault planes are randomly distributed around azimuth 110° and the dips range from 20° to 65° (see leftmost column in Figure 4). Similar conclusions as for the first experiment can be drawn. The linear method fails to retrieve the true solution when inverting data from the true fault planes, which again is explained by the misfit between the predicted shear stress magnitudes and the true ones (*cf.* right panels of Figure 3). Our method is also the only one to find the true solution in the noise free and low noise cases. However, the confidence intervals and the shape ratio distribution show that there exists another group of solutions, significantly different from the true solution, that explain this data set well (see the multiples lobes in the stereonets, and the bimodal distribution of the shape ratios in

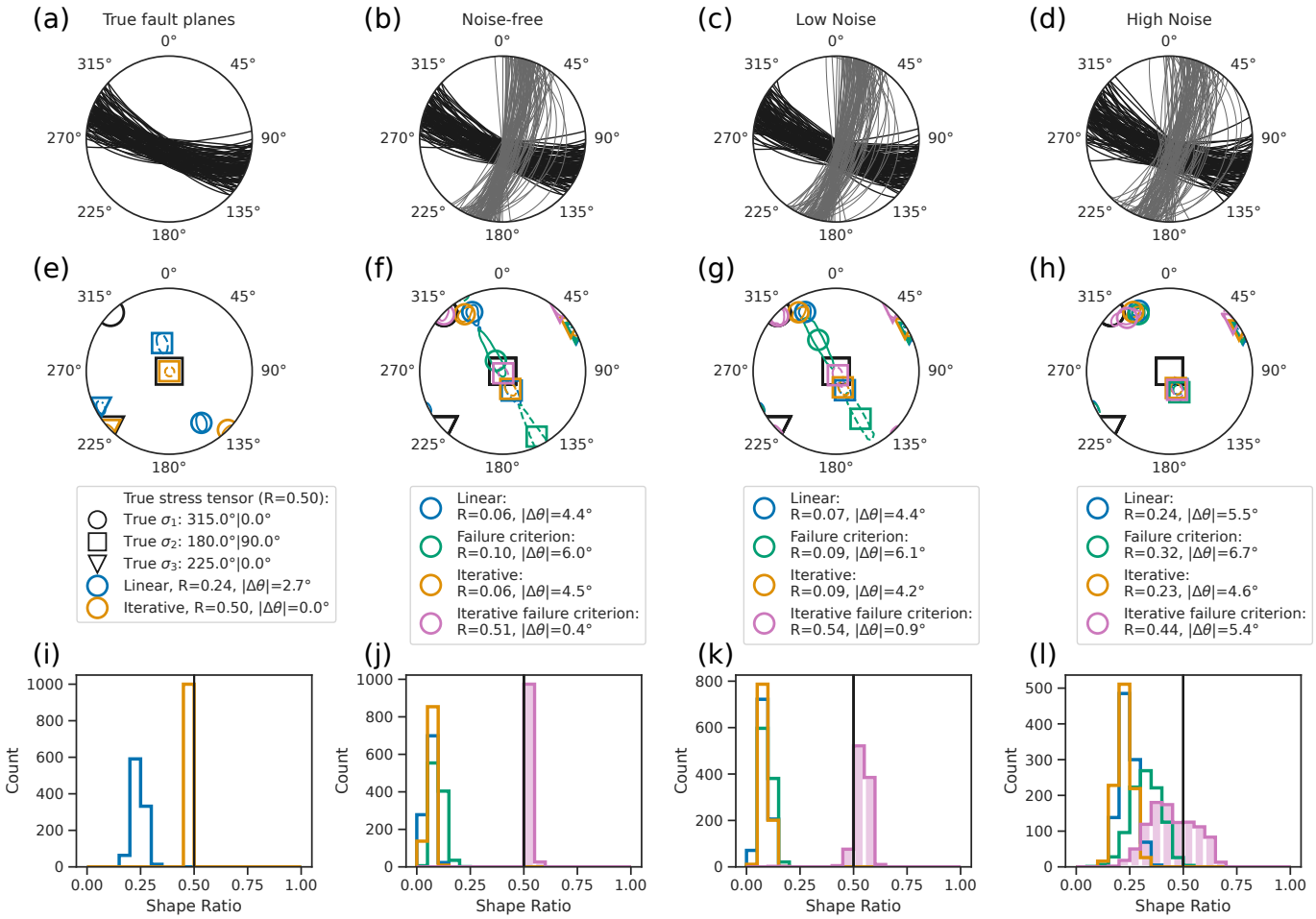

Figure 2: Synthetic experiment 1. The true stress tensor (leftmost column, middle row, large black symbols) promotes right-lateral strike-slip faulting on east-west oriented vertical faults. The shape ratio is 0.50. The fault orientations are randomly chosen from a range of parameters that is physically sensible given the stress state (see text), and the rakes are chosen such that slip is along the maximum shear stress direction. **a, e, i:** Data set with only the 100 true fault planes. **b, f, j:** Noise free data set with both the fault planes and their auxiliary planes. **c, g, k:** Data set with noisy fault planes with strikes/dips/rakes perturbed by random values in $[-3°; +3°]$, and their auxiliary planes. **d, h, i:** Data set with noisy fault planes with strikes/dips/rakes perturbed by random values in $[-10°; +10°]$, and their auxiliary planes. **a, b, c, d:** Fault planes (black lines) and auxiliary planes (grey lines). **e, f, g, h:** Lower hemisphere, equal area stereographic projections of the principal stress axes and their 95% confidence intervals (CI) estimated from 1000 bootstrap resamplings: solid lines = σ_1 CI, dashed lines = σ_2 CI, dot-dashed lines = σ_3 CI. The legend shows the inverted shape ratios R, and the mean angle $|\Delta\theta|$ between the predicted shear directions *on the true fault planes* and the true slip directions. Circles, squares and triangles are the most compressive (σ_1), intermediate (σ_2) and least compressive (σ_3) stresses, respectively. **i, j, k, l:** The distributions of shape ratios from the 1000 bootstrap resamplings. The vertical black line indices the true shape ratio. The proposed method is labeled "Iterative failure criterion" and is shaded for clarity.

Figure 4). In the high noise scenario, all methods produce solutions that are off the true solution, but our method's solution is the closest and, more importantly, it is the only method that captures the true solution inside its 95% confidence interval.

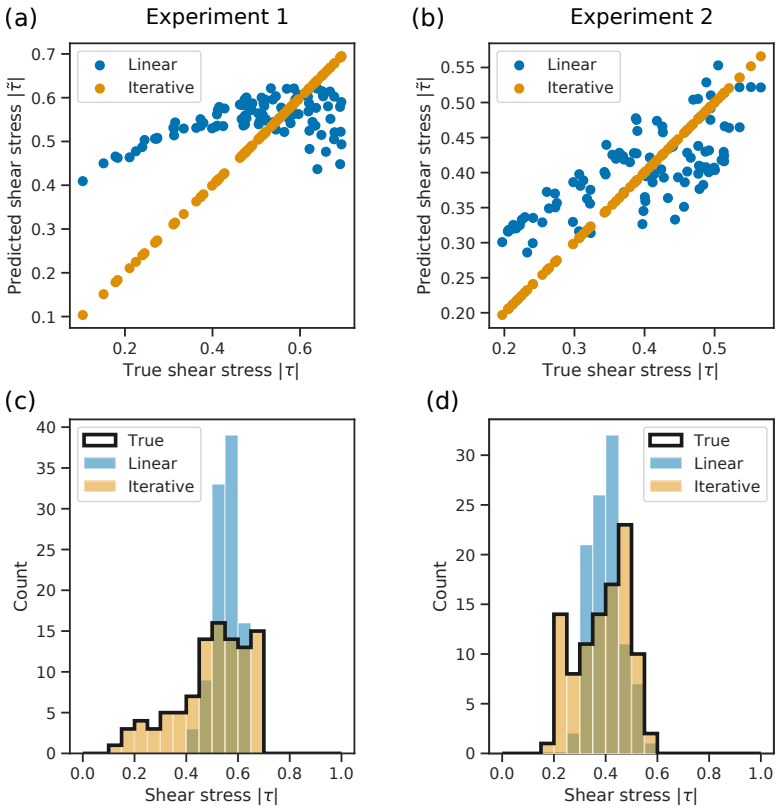

Figure 3: Predicted shear stress magnitudes. **a, c:** Synthetic experiment 1. **b, d:** Synthetic experiment 2. The linear inversion does not predict the relative shear stress magnitudes correctly, but our iterative procedure retrieves the true values.

4. Real Data Applications

4.1. Case Study 1: Central Crete

We now test our method on real data sets. The first application is on the Central Crete data set of field measurements from Angelier [1979], which was also used by Michael [1984] as a test for their linear method. In this data set the true fault planes are known since they were measured in the field (see left panel of Figure 5). The inversion results from the linear and the iterative methods are shown in Figure 5. The linear method finds a solution that is similar to the one shown in Michael [1984], and the iterative method produces a solution that is closer to the one in Angelier [1979]. Note that in the original publications, the authors use another definition of the shape ratio: $\Phi = 1 - R$. The measure of misfit $|\Delta\theta|$ shown in Figure 5 is the mean angle between predicted and observed shear traction (using the Wallace-Bott assumption). The values of $|\Delta\theta|$ obtained here are similar to those presented in Angelier [1979] and Michael [1984].

The large azimuthal uncertainty on σ_2 and σ_3 in both methods is a physical consequence of the stress state (see Figure 5 middle panel). In this tectonic setting, the two horizontal stresses σ_2 and σ_3 have close values ($R \approx 1$, uniaxial deviatoric compression). Therefore, the horizontal component of the shear traction is always much smaller than the vertical component, and the predicted shear direc-

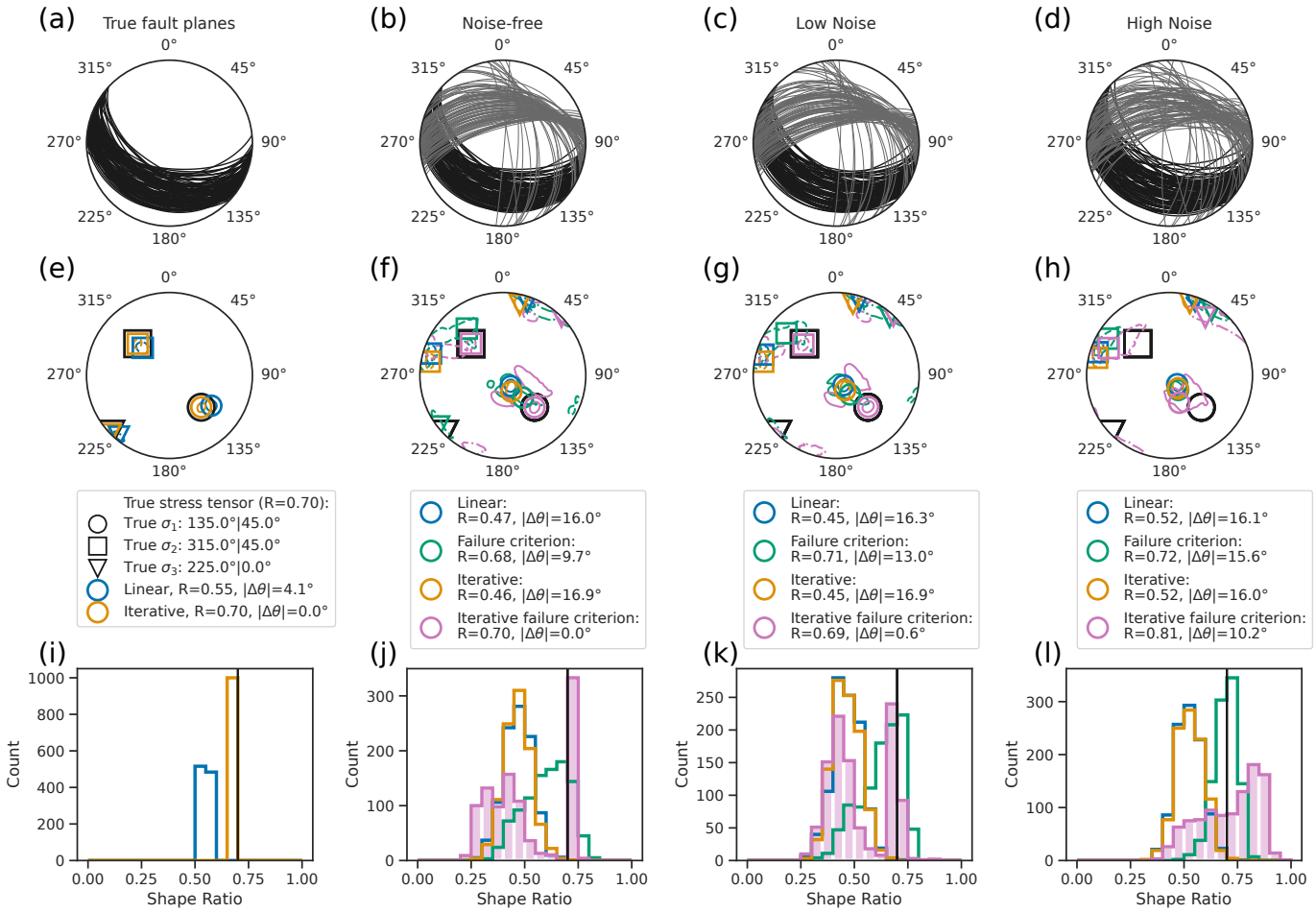

Figure 4: Synthetic experiment 2. The true stress tensor (**e**) promotes right-lateral oblique strike-slip faulting with a normal faulting component on east-west oriented faults. The shape ratio is 0.70. Same legend as Figure 2.

tions show little sensitivity to the directions of the horizontal principal stresses. Thus, the azimuths of σ_2 and σ_3 are only weakly constrained by this data set. We note that the confidence intervals estimated in Michael [1984] based on gaussian statistics are smaller than those presented in Figure 5, and failed to capture the physical lack of constraint over the directions σ_2 and σ_3 [also discussed in Michael, 1987]. This emphasizes the importance of better estimates of confidence intervals, such as via non-parametric methods. With this data set, the stress tensors inverted with the linear and the iterative methods both give shear stress magnitudes that are narrowly distributed around 0.5 (see rightmost panel of Figure 5), which explains why the linear method and the underlying assumption of constant shear stress magnitude do well.

4.2. Case Study 2: Western North Anatolian Fault

The second application is on a data set of focal mechanisms from the western North Anatolian Fault Zone, compiled in Poyraz et al. [2015]. The authors subdivided the data set into the 1999 M_w7.6 Izmit earthquake and its aftershocks (Izmit data set, 20 focal mechanisms, *cf.* bottom left

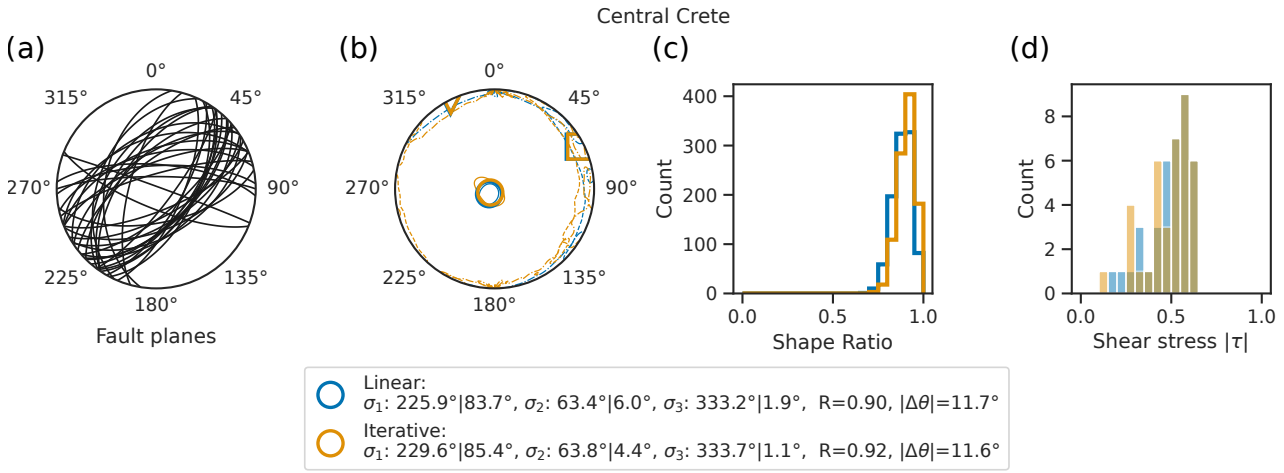

Figure 5: Inversion of the central Crete data set from Angelier [1979]. **a:** Fault plane orientations. **b:** Principal stress directions of the inverted stress tensor with the linear method due to Michael [1984] (blue symbols) and the iterative method introduced in Section 2.2. In the original publication, Angelier [1979] find similar stress directions and a shape ratio of $R = 0.93$. The 95% confidence intervals (CI) derived from 1000 bootstrapped data sets are shown: solid lines $= \sigma_1$ CI, dashed lines $= \sigma_2$ CI, dot-dashed lines $= \sigma_3$ CI. **c:** Empirical shape ratio distributions estimated from the bootstrap resampling. **d:** Distribution of shear stress magnitudes resolved on the fault planes.

panel of Figure 6), and earthquakes recorded a decade later (DANA data set, 41 focal mechanisms, *cf.* top left panel of Figure 6). They inverted both data sets with the non-linear method FMSI [Gephart, 1990] to estimate the stress tensor in the two time periods. The FMSI solutions from Poyraz et al. [2015] and the solutions obtained with the linear and the proposed iterative methods are presented in Figure 6.

In both cases, the iterative linear and failure criterion method produced solutions that are consistent with the FMSI solutions. On the DANA data set, all three methods agree well on the directions of the principal stresses, however the linear method yields a shape ratio ($R = 0.33$) that is significantly smaller than the value reported in Poyraz et al. [2015] ($R = 0.45$) and the solution of the iterative method ($R = 0.54$). The shape ratio of the regional stress tensor in the western North Anatolian Fault Zone, around the Izmit rupture, is usually estimated to be $R \approx 0.5$ [*e.g.* Kiratzi, 2002; Pınar et al., 2010]. The proposed method gives the lowest measure of angular misfit $|\Delta\theta|$, although this criterion does not allow a fair comparison with the FMSI solution since FMSI is not designed to minimize $|\Delta\theta|$, as it also considers errors in the orientation of the fault plane itself.

Uncertainties and inconsistencies between methods are larger for the Izmit data set, partly due to the low number of events (20 focal mechanisms). The low shape ratios, $R = 0.18$ with the linear method and $R = 0.38$ with the iterative method, indicate that σ_1 and σ_2 are close in magnitude. Therefore, similarly to the reason given in Section 4.1, we observe poorly constrained maximum and intermediate compression axes. The low values of shape ratio inverted for this data set reflect the mixture of strike-slip and normal faulting (transtensional regime) that followed the Izmit earthquake [*e.g.* Bohnhoff et al., 2006; Pınar et al., 2010]. Our method still produced a solution that is consistent with the FMSI solution, and the lowest $|\Delta\theta|$. Here, the FMSI solution displays a surprisingly large

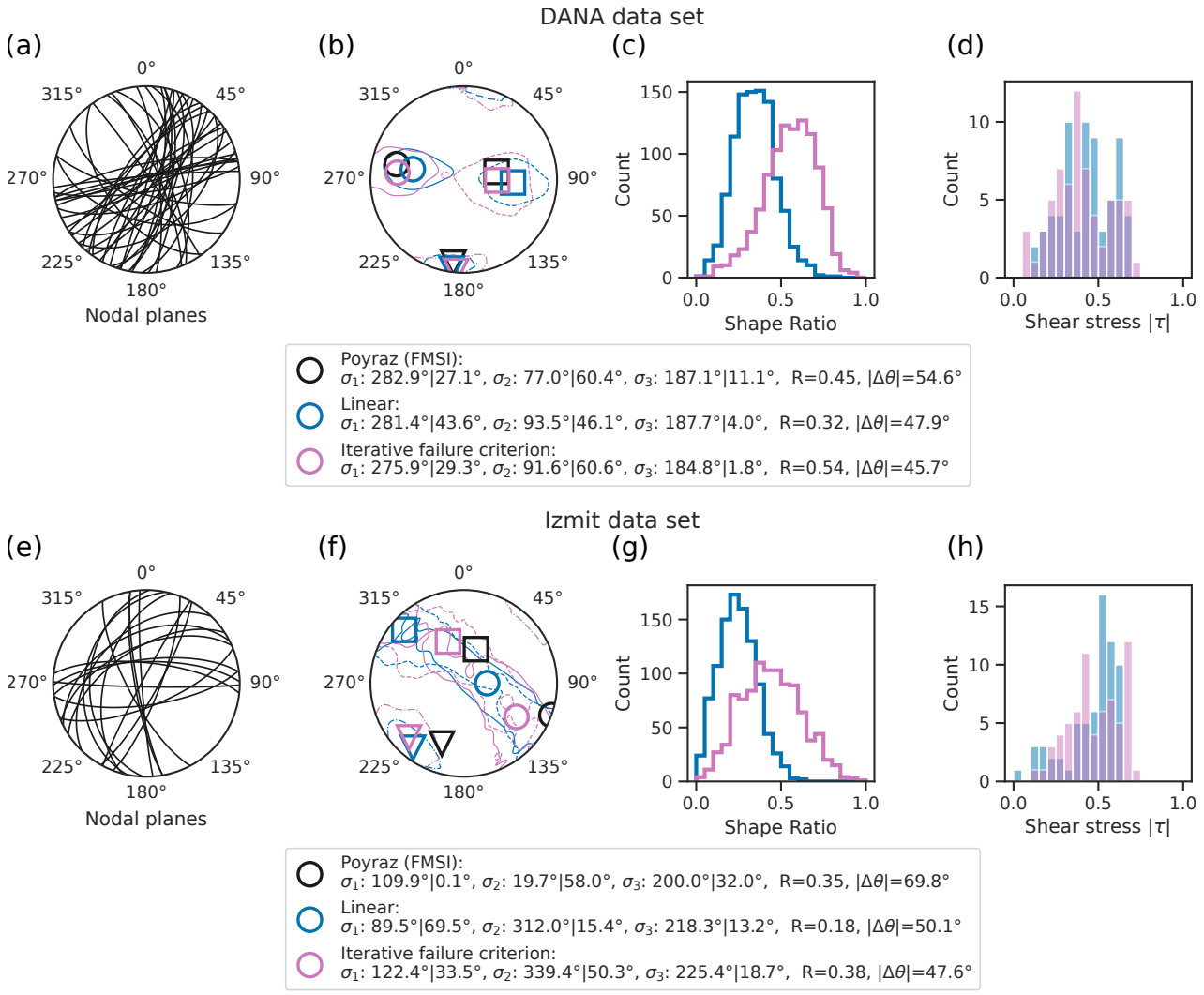

Figure 6: Inversion of the North Anatolian Fault data set from Poyraz et al. [2015]. **a, b, c, d:** Focal mechanisms from the DANA data set [Dense Array for North Anatolia DANA , 2012]. **e, f, g, h:** Focal mechanisms from the 1999-08-17 M_w7.6 Izmit earthquake and some of its aftershocks. Columns are the same as in Figure 5. The measure of misfit $|\Delta\theta|$ and the shear stress magnitudes (right panel) were computed on the fault planes selected by the instability parameter (Equations (13) and (14)).

$|\Delta\theta|$, which we speculate could be due to discrepancies between the nodal planes selected by their inversion and our failure criterion used to select the planes on which $|\Delta\theta|$ was computed.

5. Discussion on Shear Stress Magnitudes

On the North Anatolian data sets, the inverted stress tensors predict shear stress magnitudes that span a large range of values (*cf.* rightmost column of Figure 6), similarly to what we saw in the synthetic experiments (Figure 3). This shows that data sets where fault orientations are not consistent with constant shear stress do occur in practice, even though it might seem to contradict

basic physical arguments at first. Michael [1984] justified the assumption of constant shear stress with the Mohr-Coulomb failure criterion (Equation (13), with cohesion $C = 0$): given that normal stress is mostly controlled by the lithostatic stress, it has no reason to vary significantly with the fault orientation. Following this reasoning, the only variable left for explaining a wide range of shear stress magnitudes, as shown in Figures 3 and 6, is the coefficient of friction μ at the time of failure, which was shown to exhibit little variation in rock samples [0.6-0.85, Byerlee, 1978]. However, the previous arguments disregard the importance of pore fluid pressure on controlling the effective normal stress at play in the Mohr-Coulomb failure criterion [Faulkner et al., 2006], and the fact that real faults might have coefficients of friction as low as 0.2 due to various reasons, such as the presence of weak minerals or rock fabric [Collettini et al., 2009].

The wide distribution of shear stress magnitudes (in particular, the low values) is indicative of the presence of non-optimally oriented faults in the inverted *average* stress tensor. Rupture on these non-optimally oriented faults can be explained by weakness due to low friction coefficient or high pore fluid pressure, or by heterogeneities in the stress field (*e.g.* interactions between faults). In fact, interactions between applied stress and resulting structures develop local heterogeneities in the stress field, which can lead to the appearance of complex structures [*e.g.* Riedel shears, Dresen, 1991]. In the latter case, fault misorientation is an artifact of the assumption of uniform stress field. Either for real (weak faults) or artificial (invalidity of the uniform stress assumption) reasons, these non-optimally oriented faults are found in data sets in general. By iteratively inverting for the shear stress magnitudes (see Equations (8)-(10)), our method learns to identify these non-optimally oriented faults and adjusts the right-hand side of Equation (5) accordingly ($d_i^{(t)} = \tau_i^{(t)} d^{(0)}$, *cf.* Equation (9)) in order to achieve low residuals $(d - Gm)^2$ on these faults. Under the assumption of constant shear stress magnitude, the linear method is forced to find a solution that produces neither a good solution on the optimally oriented faults nor on the non-optimally oriented faults (see left column of Figure 2) as a consequence of the least-squares criterion. The identification of non-optimally oriented faults combined with bootstrap resampling is likely to produce more realistic estimates of uncertainties due to violations of the uniform stress assumption than the linear method.

6. Summary and Concluding Remarks

In Section 2.1, we introduced the stress tensor inversion problem and presented the underlying assumptions and drawbacks. In Section 2.2, we introduced an iterative inversion method built upon the linear inversion due to Michael [1984], and described how to combine it with a Mohr-Coulomb failure criterion [*e.g.* Lund and Slunga, 1999; Vavryčuk et al., 2013] to deal with focal mechanism data sets where the true fault planes are generally unknown. We used synthetic examples (Section 3) to demonstrate the efficacy of our method, its advantages with respect to the linear inversion, and its potential to estimate confidence intervals with the bootstrap resampling method [Efron and Tibshirani, 1986]. We then validated the proposed method on real data sets (Section 4).

The first data set was constituted of field measurements from Central Crete and was inverted in Angelier [1979] and Michael [1984], with which we showed that the proposed method gave consistent results, and more accurate confidence intervals. The second data set was made of focal mechanisms

from earthquakes located along the western section of the North Anatolian Fault Zone. We compared our method against the results presented in Poyraz et al. [2015] that were obtained with the FMSI software that is considered the state-of-the-art stress inversion method [Gephart and Forsyth, 1984; Gephart, 1990]. We showed that the solution produced by our method was in good agreement with the FMSI solution, whereas the linear method gave stress tensors with significantly different shape ratios.

Finally, in Section 5, we discussed the implications of the assumption of constant shear stress magnitudes. We explained that relaxing the assumption on shear stress magnitudes helps our method deal with non-optimally oriented faults that are either symptomatic of stress heterogeneity (*i.e.* violations of the uniform stress assumption) or of fault weakness. Therefore, we believe that the inversion method proposed here produces accurate solutions, is easy to implement, and is fast enough to allow accurate estimates of uncertainties with non-parametric methods, such the bootstrap resampling method.

The stress inversion method introduced in this article can be implemented using our Python package ILSI (see Data and Resources).

Data and Resources

The first case study uses the Central Crete data set published in Angelier [1979] (their Table 1), and the second case study uses the North Anatolian data set published in Poyraz et al. [2015] (their Table 2).

The Python package ILSI, available at `https://github.com/ebeauce/ILSI`, implements the method proposed here and provides tutorial scripts to reproduce our figures (version 1.0.0, last accessed July 2021).

Acknowledgements

This project has received funding from the European Research Council (ERC) under the European Union's Horizon H2020 research and innovation program (grant agreement No 742335). E.B. was also supported by funds associated with Robert D. van der Hilst's Schlumberger chair.

References

J. Angelier. Determination of the mean principal directions of stresses for a given fault population. *Tectonophysics*, 56(3-4):T17–T26, 1979.

J. Angelier, A. Tarantola, B. Valette, and S. Manoussis. Inversion of field data in fault tectonics to obtain the regional stress—i. single phase fault populations: a new method of computing the stress tensor. *Geophysical Journal International*, 69(3):607–621, 1982.

M. Bohnhoff, H. Grosser, and G. Dresen. Strain partitioning and stress rotation at the North Anatolian fault zone from aftershock focal mechanisms of the 1999 Izmit m w= 7.4 earthquake. *Geophysical Journal International*, 166(1):373–385, 2006.

M. H. P. Bott. The mechanics of oblique slip faulting. *Geological magazine*, 96(2):109–117, 1959.

J. Byerlee. Friction of rocks. In *Rock friction and earthquake prediction*, pages 615–626. Springer, 1978.

E. Carey et al. Analyse theorique et numerique d'un modele mecanique elementaire applique a l'etude d'une population de failles. 1974.

C. Collettini, A. Niemeijer, C. Viti, and C. Marone. Fault zone fabric and fault weakness. *Nature*, 462(7275):907–910, 2009.

DANA . Dense array for north anatolia, 2012. URL `http://www.fdsn.org/doi/10.7914/SN/YH_2012`.

G. Dresen. Stress distribution and the orientation of riedel shears. *Tectonophysics*, 188(3-4):239–247, 1991.

B. Efron and R. Tibshirani. Bootstrap methods for standard errors, confidence intervals, and other measures of statistical accuracy. *Statistical science*, pages 54–75, 1986.

D. Faulkner, T. Mitchell, D. Healy, and M. Heap. Slip on'weak'faults by the rotation of regional stress in the fracture damage zone. *Nature*, 444(7121):922–925, 2006.

J. W. Gephart. Fmsi: A fortran program for inverting fault/slickenside and earthquake focal mechanism data to obtain the regional stress tensor. *Computers & Geosciences*, 16(7):953–989, 1990.

J. W. Gephart and D. W. Forsyth. An improved method for determining the regional stress tensor using earthquake focal mechanism data: application to the san fernando earthquake sequence. *Journal of Geophysical Research: Solid Earth*, 89(B11):9305–9320, 1984.

J. L. Hardebeck and A. J. Michael. Damped regional-scale stress inversions: Methodology and examples for southern california and the coalinga aftershock sequence. *Journal of Geophysical Research: Solid Earth*, 111(B11), 2006.

A. A. Kiratzi. Stress tensor inversions along the westernmost North Anatolian Fault Zone and its continuation into the North Aegean Sea. *Geophysical Journal International*, 151(2):360–376, 2002.

B. Lund and R. Slunga. Stress tensor inversion using detailed microearthquake information and stability constraints: Application to ölfus in southwest iceland. *Journal of Geophysical Research: Solid Earth*, 104(B7):14947–14964, 1999.

P. Martínez-Garzón, G. Kwiatek, M. Ickrath, and M. Bohnhoff. Msatsi: A matlab package for stress inversion combining solid classic methodology, a new simplified user-handling, and a visualization tool. *Seismological Research Letters*, 85(4):896–904, 2014.

A. J. Michael. Determination of stress from slip data: faults and folds. *Journal of Geophysical Research: Solid Earth*, 89(B13):11517–11526, 1984.

A. J. Michael. Use of focal mechanisms to determine stress: a control study. *Journal of Geophysical Research: Solid Earth*, 92(B1):357–368, 1987.

A. Pınar, S. Üçer, Y. Honkura, N. Sezgin, A. Ito, Ş. Barış, D. Kalafat, M. Matsushima, and S. Horiuchi. Spatial variation of the stress field along the fault rupture zone of the 1999 Izmit earthquake. *Earth, planets and space*, 62(3):237–256, 2010.

S. A. Poyraz, M. U. Teoman, N. Türkelli, M. Kahraman, D. Cambaz, A. Mutlu, S. Rost, G. A. Houseman, D. A. Thompson, D. Cornwell, et al. New constraints on micro-seismicity and stress state in the western part of the north anatolian fault zone: Observations from a dense seismic array. *Tectonophysics*, 656:190–201, 2015.

S. Stein and M. Wysession. *An introduction to seismology, earthquakes, and earth structure*. John Wiley & Sons, 2009.

A. Tarantola and B. Valette. Generalized nonlinear inverse problems solved using the least squares criterion. *Reviews of Geophysics*, 20(2):219–232, 1982.

V. Vavryčuk. Iterative joint inversion for stress and fault orientations from focal mechanisms. *Geophysical Journal International*, 199(1):69–77, 2014.

V. Vavryčuk, F. Bouchaala, and T. Fischer. High-resolution fault image from accurate locations and focal mechanisms of the 2008 swarm earthquakes in west bohemia, czech republic. *Tectonophysics*, 590:189–195, 2013.

R. E. Wallace. Geometry of shearing stress and relation to faulting. *The Journal of geology*, 59(2): 118–130, 1951.

Appendix A. Stress Tensor Sign Convention

Let us consider a stress tensor with northwest/southeast maximum compression and southwest/northeast minimum compression, and intermediate compression in the vertical direction (see Figure A.7). The direction of the principal stresses $\hat{\sigma}_i$ (i=1 maximum compression, i=3 minimum compression) are, in the (x, y, z)=(north, west, upward) coordinate system:

$$\hat{\sigma}_1 = \begin{pmatrix} -\frac{1}{\sqrt{2}} \\ -\frac{1}{\sqrt{2}} \\ 0 \end{pmatrix}, \quad \hat{\sigma_2} = \begin{pmatrix} 0 \\ 0 \\ 1 \end{pmatrix}, \quad \hat{\sigma}_3 = \begin{pmatrix} -\frac{1}{\sqrt{2}} \\ \frac{1}{\sqrt{2}} \\ 0 \end{pmatrix}. \tag{A.1}$$

The eigendecomposition of the stress tensor σ is:

$$\sigma = V \Sigma V^T, \tag{A.2}$$

where V is the matrix of column eigenvectors, and Σ is the diagonal matrix of eigenvalues (σ_1, σ_2, σ_3):

$$V = \begin{pmatrix} -\frac{1}{\sqrt{2}} & 0 & -\frac{1}{\sqrt{2}} \\ -\frac{1}{\sqrt{2}} & 0 & \frac{1}{\sqrt{2}} \\ 0 & 1 & 0 \end{pmatrix}; \qquad \Sigma = \begin{pmatrix} \sigma_1 & 0 & 0 \\ 0 & \sigma_2 & 0 \\ 0 & 0 & \sigma_3 \end{pmatrix}. \tag{A.3}$$

We parameterize the stress tensor by:

$$\sigma_1 = \pm 1, \quad \sigma_2 = \pm(1 - 2R), \quad \sigma_3 = \mp 1, \quad R = \frac{\sigma_1 - \sigma_2}{\sigma_1 - \sigma_3}. \tag{A.4}$$

In Equation (A.4), the upper and lower signs hold for the compression positive convention and the tension positive convention, respectively. The parameter R is called the shape ratio, it characterizes the relative magnitudes of the principal stresses. The compression positive (cp) and tension positive (tp) stress tensors are:

$$\sigma^{\mathrm{cp/tp}} = V \Sigma^{\mathrm{cp/tp}} V^T. \tag{A.5}$$

We consider the outward normal of the northern wall or, equivalently, the inward normal of the southern wall:

$$\hat{n} = \begin{pmatrix} -1 \\ 0 \\ 0 \end{pmatrix}. \tag{A.6}$$

The unitary slip of the southern wall with respect to the northern wall is (right-lateral, the southern wall moves to the west):

$$\hat{d} = \begin{pmatrix} 0 \\ +1 \\ 0 \end{pmatrix}. \tag{A.7}$$

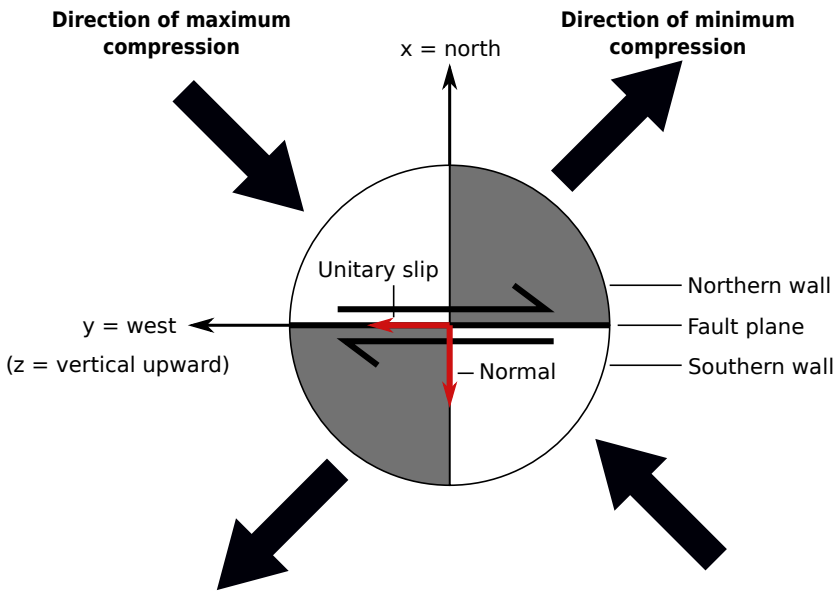

Figure A.7: East-west right-lateral strike-slip fault under northwest-southeast maximum compression and southwest-northeast minimum compression. The intermediate stress is vertical.

Appendix A.1. Compression Positive

$$\sigma^{\mathrm{cp}} = V\Sigma^{\mathrm{cp}}V^T = \begin{pmatrix} 0 & +1 & 0 \\ +1 & 0 & 0 \\ 0 & 0 & 0 \end{pmatrix} \tag{A.8}$$

Compression is positive when defining the elements of the stress tensor for *inward* pointing normals. Therefore, the normal defined by Equation (A.6) is the inward normal of the southern wall, and $\sigma^{\mathrm{cp}}\hat{n}$ gives the traction on the *southern* wall:

$$t(\hat{n}) = \sigma^{\mathrm{cp}}\hat{n} = \begin{pmatrix} 0 \\ -1 \\ 0 \end{pmatrix}. \tag{A.9}$$

The traction on the southern wall is $-1\hat{y}$, *i.e.* it points in the east direction, which is opposite to the direction of motion of the southern wall with respect to the northern wall.

Appendix A.2. Tension Positive

$$\sigma^{\mathrm{tp}} = V\Sigma^{\mathrm{tp}}V^T = \begin{pmatrix} 0 & -1 & 0 \\ -1 & 0 & 0 \\ 0 & 0 & 0 \end{pmatrix} \tag{A.10}$$

Tension is positive when defining the elements of the stress tensor for *outward* pointing normals (common definition of the Cauchy stress tensor in physics). Therefore, the normal defined by Equation (A.6) is the outward normal of the northern wall, and $\sigma^{\mathrm{tp}}\hat{n}$ gives the traction on the *northern*

wall:

$$t(\hat{n}) = \sigma^{\mathrm{tp}}\hat{n} = \begin{pmatrix} 0 \\ +1 \\ 0 \end{pmatrix}. \tag{A.11}$$

The traction on the southern wall is $+1\hat{y}$, *i.e.* it points in the west direction, which is the direction of motion of the southern wall with respect to the northern wall.

Appendix A.3. Implications for the Stress Tensor Inversion

This simple example shows that, given the coordinate system we chose (x, y, z = north, west, upward), outward pointing normals of the footwalls and slip directions of the hanging walls with respect to footwalls are consistent with the tension positive convention. The inward pointing normals of the hanging walls and slip directions of the footwall with respect to hanging walls are consistent with the compression positive convention.